Nanoscale

Accepted Manuscript

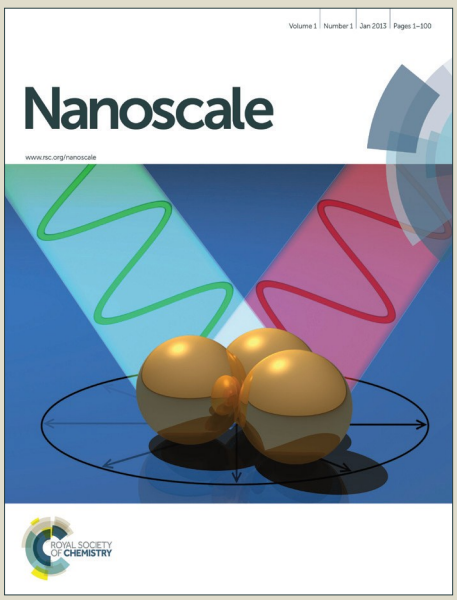

ROYAL SOCIETY OF CHEMISTRY

www.rsc.org/nanoscale

Nanoscale

ARTICLE

High Sensitive and Fast Phototransistor Based on Large Size CVD-grown SnS_2 Nanosheets

Received 00th January 20xx,
Accepted 00th January 20xx

DOI: 10.1039/x0xx00000x

www.rsc.org/

Yun Huang, [a] Hui-Xiong Deng, [b] Kai Xu, [a] Zhen-Xing Wang, [a] Qi-Sheng Wang, [a] Feng-Mei Wang, [a] Feng Wang, [a] Xue-Ying Zhan, [a] Shu-Shen Li, [b] Jun-Wei Luo [b,c,*] and Jun He [a,*]

A facile and fertile CVD method is reported for the first time, to synthesize high-quality hexagonal SnS_2 nanosheets on carbo cloth via in-situ sulfurization of SnO_2. Moreover, high sensitive phototransistors based on SnS_2 with on/off ratio surpassin 10^6 in ambient and a rising time as short as 22 ms in vacuum are fabricated, which are superior than most phototransistor based on LMDs. Electrical transport measurements at varied temperatures together with theoretical calculations verify tha sulfur vacancy generated by the growth process would induce a defect level near the bottom of conduct band, w significantly affect the performance of SnS_2 device. These findings may open up a new roadway for the synthesis of LMDs. shed light on defects effects on devices and expand the building blocks for high performance optoelectronic devices.

Introduction

Two-dimensional (2D) layered materials have become intriguing building blocks during the last few years for their superior structures compared to their bulk counterparts.[1, 2] The atomically ultrathin thickness and absence of surface dangling bonds render them as potential candidates for high-performance electronic and optoelectronic devices at nanoscale.[3, 4] As a representative, graphene has been enthusiastically studied by researchers for its superior properties such as ultrahigh electron mobility, single-layer stability and large-scale producibility.[5, 6] However, the intrinsic gapless characteristic impedes itself for applications in digital electronics. Layered metal dichalcogenides (LMDs), which complement graphene with sizable band gaps, gradually become the focus of material researches. Plenty of gorgeous works based on LMDs like MoS_2, WSe_2, GaTe have been reported for applications of electronic and photoelectronic in recent years.[7-14] For example, monolayer MoS_2 FET have shown a high carrier and on/off ratio larger than 10^8.[15] Monolayer WSe_2 realizes an atomic p-n diode at the ultimate thickness limit.[16]

However, for practical applications, there are still great challenges in LMD-based devices, such as large-scale growth, CMOS-compatible device fabrication, and high photoelectric performance as well. Motivated by these points, we start to explore a new kind of LMDs. As a member of them, tin disulfide (SnS_2), owning a similar lattice type with MoS_2 and a larger ban gap of 2.1 eV,[17] which is advantageous for suppressing source to drain tunneling in application of short channel MOSFETs.[18] intensely interest us not only for its potential superior properties, but also for its nature of earth abundance and environmental friendly. So far, as general methods for i synthesis, solvothermal process and mechanical exfoliation fai to synthesize single-crystal SnS_2 with high yield and larg scale.[19-21] On the other hand, chemical vapor deposition (CVD) has been proved to be a successful method to synthesize high quality LMDs, such as MoS_2 and WSe_2, [22-24] indicating the possibility of it to efficiently grow SnS_2. However, only fe works have been reported to synthesize SnS_2 NSs via CVD method in very recent. Peng et al. grew SnS_2 NSs on seeded SiO_2/Si substrates and demonstrated their application as fa photodetectors with response time ≈ 5 μs.[25] Xia et al. certified a screw-dislocation-driven spiral growth process of SnS_2 NSs on mica and demonstrated their high performance a photodetectors.[26] Further studies focusing on their large scale production and optoelectronic properties are still in need. Another issue worth to be noted is that defects in the layered structures, which are easily induced during the synthesis process, might affect the device performance significantly. T date, only a few of systematical works have been carried out to shed light on it, making this issue an intriguing one. In fact, b developing a low temperature thiol chemistry route to repair the sulfur vacancy of MoS_2,[27-29] the carrier mobility can b raised from 7.7 $cm^2 V^{-1}s^{-1}$ to 80 $cm^2 V^{-1}s^{-1}$. Similarly, the on/off ratio of GaTe FET can be dramatically enhanced by depressing Ga vacancy activity at low temperature.[7] These achievements strongly encourage us to elucidate the impacts of defects i LMDs like SnS_2.

Herein, we develop a facile and fertile CVD method, for the first time, to synthesize hexagonal SnS_2 NSs on carbon cloth

[a] CAS Key Laboratory of Nanosystem and Hierarchical Fabrication, National Center for Nanoscience and Technology, 100190, Beijing, P. R. China
[b] State key laboratory of superlattices and microstructures, Institute of Semiconductors, Chinese Academy of Sciences, 100083, Beijing, P.R. China
[c] Synergetic Innovation Center of Quantum Information and Quantum Physics, University of Science and Technology of China, Hefei, Anhui 230026, China
E-mail: hej@nanoctr.cn, jwluo@semi.ac.cn
Electronic Supplementary Information (ESI) available: [details of any supplementary information available should be included here]. See DOI: 10.1039/x0xx00000x

characterizations clearly indicate the as-grown SnS_2 NSs own high crystalline, uniform thickness and large scale. Back-gated SnS_2 phototransistors are fabricated with a high on/off ratio≈ 1.7×10^6 in ambient and a fast rising time less than 22 ms in vacuum, which are comparable, even better than mechanically exfoliated SnS_2 membranes and many other 2D materials in a back gated transistor structure. [15, 30-36] Furthermore, electrical measurements at various temperatures (80 K - 290 K) and first-principles calculation are conducted to study the effect of defects. Charge density extracted from Id-Vg curves dramatically increases at temperatures higher than 180 K, indicating there exists a thermal excitation activity. The activation energy 118±5.31 meV speculated from R-T curves agrees well with the theoretical calculated 199 meV transition energy of the defect level induced by sulfur vacancy. Our study may supply an effective method to synthesize new layered metal dichalcogenides and open opportunities to explore new type phototransistors.

Results and discussion

As shown in Fig. 1a, SnS_2 has a sandwich structure with a layer of Sn atoms embedded between two layers of S atoms. Such array of atoms renders it a super symmetrical structure which can be embodied in the hexagonal shape of as-grown SnS_2 NS with its selected area electron diffraction (SAED) pattern of TEM depicted in Fig. 1d and e, respectively. Typically, SnS_2 NSs could be obtained through a two-step CVD method in a horizontal two-zone vacuum tube furnace. Firstly, we grow large-scale SnO_2 nanowire arrays on carbon cloth using a modified method in ref 19.[20] Secondly, we synthesize SnS_2 NSs via in-situ sulfurization of SnO_2 nanowires (see Supporting Information: Experimental Section for details). These SnO_2 nanowires with large specific surface area may serve as pure, homogeneous source materials during the sulfuration process, which supply the growth of high crystalline SnS_2 NSs. The experimental setup and the growth process of SnS_2 are schematically illustrated in Fig. S1 (Supporting Information).

The SEM images of Fig. S2a and b (Supporting Information) demonstrate that SnO_2 nanowires can be effectively converted to SnS_2 NSs. Fig. 1b shows an atomic force microscope (AFM) image of a semi-hexagonal SnS_2 NS with a thickness of 16.6 nm. Most grown hexagonal NSs are uniform and flattened with lateral size of a few micrometers and the thickness varying from 15 to 200 nm. Raman spectroscopy is used to confirm the grown NSs of SnS_2. As illustrated in Fig. 1c, an intense Raman peak at 313.6 cm^{-1} corresponding to the typical A_{1g} mode for SnS_2.[37] The component analysis can be further verified by the energy dispersive X-ray (EDX) spectroscopy, demonstrated in Fig. S2c (Supporting Information). Fig. 1d displays a TEM image of a semi-hexagonal SnS_2 NS dispersed onto a holey carbon grid. High crystallinity of this SnS_2 NS could easily be concluded from the regular diffraction fringes (HRTEM, Fig. 1e) and the corresponding diffraction pattern (SAED, inset of Fig. 1e), with the lattice spacing of 3.18 Å indexed to (100) plane. All the characterizing results confirm that our CVD method can

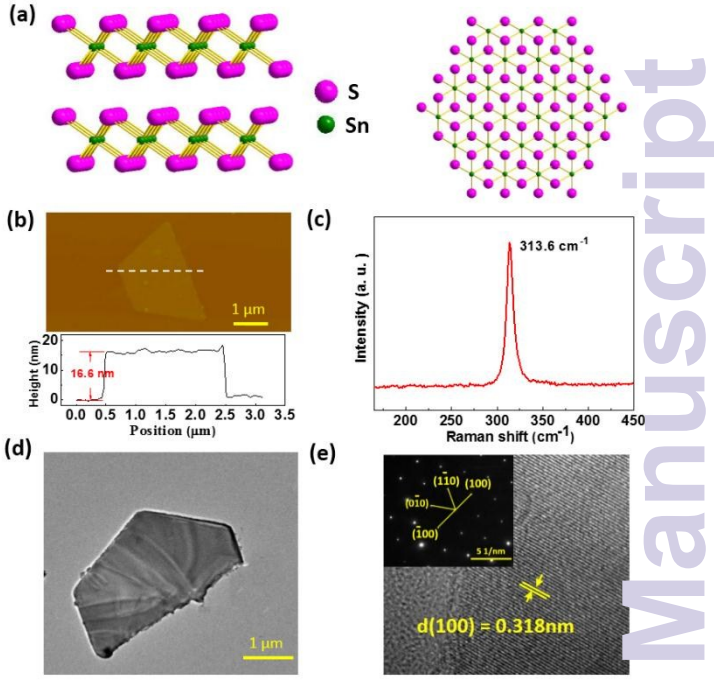

Fig. 1 Schemes and characterization of SnS_2 NSs. (a) Side view and top view of the schematic SnS_2 structures with purple and green balls stands for S and Sn atoms respectively. (b) AFM image along with cross section height profiles of a semi-hexagonal SnS_2 NSs ~ 16.6 nm thick. (c) Raman spectra of SnS_2 NSs with an excitation laser of 532 nm. (d) Low magnification bright field TEM image and (e) HRTEM image of a typical SnS_2 NSs. Inset: the corresponding SEAD image.

successfully synthesize high quality SnS_2 NSs in large scale and with uniform surface.

In order to evaluate the electrical characteristics of our SnS_2 NSs, back-gated FET devices are fabricated through a standard electron beam lithography (EBL) process followed by thermal deposition of Cr/Au (8 nm/60 nm) as electrodes. Fig. 2a presents the AFM image of our device with the channel thickness ≈35 nm,channel length and channel width ≈2.7 μm and ≈3.5 μm, respectively. The transfer curve depicted in Fig. 2b displays obvious n-type conducting behavior and a high on/off ratio surpassing 10^6 in ambient. Noted that the environmental conditions like atmosphere or temperature have a strong effect on electrical properties of most layered materials,[7, 14] we therefore put our device in vacuum and measure its transport characteristics at low temperatures in order to elucidate these effects. Fig. S3a (Supporting Information) contrasts its I_d-V curves in ambient and vacuum. It is worth noting that when measuring in vacuum, the off state current is much higher than that in ambient while the on state current almost keeps the same, leading to the on/off ratio dropping by nearly 4 orders of magnitude. This phenomenon is commonly explained by the effect of gas adsorption,[5] which can also be verified by the threshold voltage (V_{th}) shifting from 7 V to 10 V, from vacuum to ambient. Besides, the different behavior of light response in ambient and vacuum also confirm the effect of oxygen adsorption, which would be discussed later.

To better understand how temperature affects the performance of FET, we carry out a series of measurements from room temperature (290 K) to liquid nitrogen temperature (77 K). All transfer curves are measured under 3 V bias volta

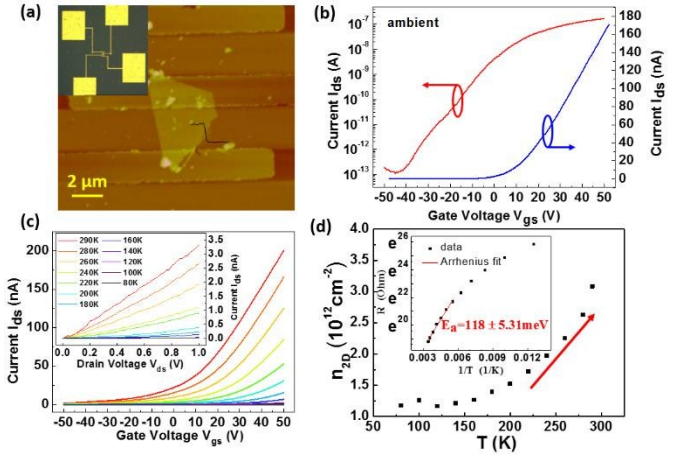

Fig. 2 FET based on SnS_2 NSs and its temperature dependent properties. (a) AFM image of the high performance FET based on SnS_2 NSs. Inset: the optical image of the same device. (b) Transfer curves in logarithmic and linear coordinates under 3 V bias voltage in ambient. (c) Transfer curves at varied temperatures from 80 K to 290 K in vacuum. Inset: corresponding I_{ds}-V_{ds} curves. (d) Charge concentration as a function of temperature at V_{gs} = 50 V. Inset: Arrhenius plot of the resistance of the same device.

and output characteristics curves are measured under zero gate voltage. As shown in the inset of Fig. 2c, the nearly linear I_d-V_d curves in the whole temperature range imply our devices own ideal ohmic contacts. By linear fitting I_d-V_g curve in Fig. 2c, we can deduce the 2D charge density (n_{2D}) from equation:[15]

$$n_{2D} = C_{ox}\Delta V_{bg}/e, \qquad (1)$$

where $C_{ox} = \varepsilon_0\varepsilon_r/d_{ox}$, $\varepsilon_0 = 8.85\times10^{-12}\ Fm^{-1}$, $\varepsilon_r = 3.9$, $d_{ox} = 300\ nm$, $e = 1.6\times10^{-19}\ C$, $\Delta V_{bg} = V_{bg} - V_{bg,th}$. Fig. 2d presents the relationship between n_{2D} and temperature at V_g = 50 V. Obviously, this relationship has a turning point at ≈180 K, embodying in n_{2D} sharply increases at temperatures above 180 K. I_d-V_g curves at varied temperatures in logarithmic coordinate (Fig. S3b, Supporting Information) also exhibit a similar behavior as the off state currents sharply increase at temperatures above 180 K. This tendency indicates that low temperature would inhibit thermally excited carriers so that the conductivity of the device reduces as the temperature decreases. The activation behavior shown in Fig. 2d can be further validated by linear fitting R_T-T curve using the Arrhenius equation:[38]

$$R_T = 1/G = (1/G_0)e^{E_a/k_BT}, \qquad (2)$$

where R_T are resistances at the measuring temperature T, E_a is the thermal activation energy, k_B is the Boltzman constant and G_0 stands for the temperature-dependent parameter extracted from the fitting curves. In fact, the measured data fit the equation quite well and an activation energy of 118±5.31 meV can be concluded from the plots (180 to 290 K). There are two possible reasons for this thermal excitation behavior: contact barrier and defect induced doping effects.[39] In the inset of Fig. 2c, I_{ds}-V_{ds} curves at varied temperature are displayed. It is obvious that all the curves are linear, indicating the ohmic contact of the device. Thus, the contact barrier should be small enough to be neglected. Therefore, the activated behavior should be explained by the presence of defects induced doping levels.

To look into the dominant defects and their doping effects on SnS_2 NSs, first-principles calculations are conducted (see detailed calculation method in Experimental Section). Fig. 3a and b respectively depict the calculated formation energy and their corresponding electronic structures for possible point defects. It is obvious that sulfur vacancy (V_S), Sn-on-S anti-site defect (Sn_S) and Sn interstitial defect (Sn_i) own relative lower formation energy and behave like donors, which could be the possible reasons to explain the n-type conducting behavior of the device. Fig. 3c shows the calculated defect transition energy needed to excite an electron (hole) from the defect level to the conduction (valence) band of SnS_2 in Sn-rich environment. Considering the general deviation of calculations, both 199 meV transition energy of sulfur vacancy and 168 meV of Sn-on-S anti-site defect agree with our experimental result of 118±5.31 meV quite well. However, we believe it is sulfur vacancy that leads to the temperature-related activated behavior for its lowest formation energy among various investigated defects in most synthetic environment, from Sn-rich to S-rich. Actually, there are researches indicating sulfur vacancy in MoS_2 owning similar effects on FET devices. [28, 29]

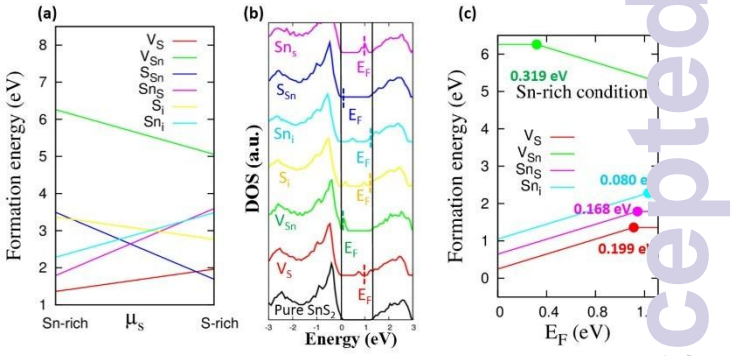

Fig. 3 First-principles DFT calculated defect results. (a)Formation energies of possible point defects in monolayer SnS_2, as function of S chemical potential: Calculated defects include S and Sn vacancies (V_s and V_{Sn}), S-on-Sn and Sn-on-S anti-site defects (S_{Sn} and Sn_S), S and Sn interstitial defects (S_i and Sn_i). (b) DOS of pure SnS_2 and for systems of SnS_2 containing respective possible defects. (c) Calculated transition energies of possible defects in Sn-rich condition.

To further study how sulfur vacancies affect the performance of SnS_2 phototransistors, we characterize our device under continuous illumination of 473 nm laser. Impressively, it shows a fast rising time ≈22 ms (Fig. 4e, inset), a decay time ≈ 11 ms (Fig. 5a, Supporting Information) and linear photocurrent increasing with the illumination intensity. As illustrated in Fig. 4a and b, the drain currents remarkably increase with the enhancement of the incident light power, indicating our device is a sensitive phototransistor. Fig. 4b shows that currents in the off state are more sensitive to the power density of illumination which could be easily explained by the effect of Schottky barrier modulation by gate voltages.[6, 34, 37] As depicted in Fig. S4, the Schottky barrier lowers as the gate voltage increases, leading to the enhancement of current extraction by applied bias voltage and smaller proportion of photocurrents in the channel. Fig. 4c plots the On/Off (currents with/without illumination) ratio as a function of gate voltage at different powers of incident light. Obviously, the On/Off ratio decreases as the gate volt

increases and reach a highest value of 10^4 with the power of inciednt light 715 W/m^2, V_{gs} = -40 V, indicating its ultrasensitive photoswich properties. Besides, the square wave shaped *I-t* curves displayed in Fig. 4d further verify this potential whether in ambient or vacuum. Table S1 lists the characteristics of phototransistors based on typical 2D materials, which indicates the superiority of our SnS_2 phototransistor. However, it manifests a larger rising time of 0.33 s (Fig. S5b, Supporting Information) and a larger decay time of 0.13 s in ambient (Fig.5c, Supporting Information). Previous researches have indicated gases adsorbed on the surface of devices would lead to a longer response time[5, 14] and the larger currents in vacuum than that in ambient also confirm the adsorption of oxygen. Thus, the varied response time should be attributed to gas adsorption on surface rather than the instability of this material.

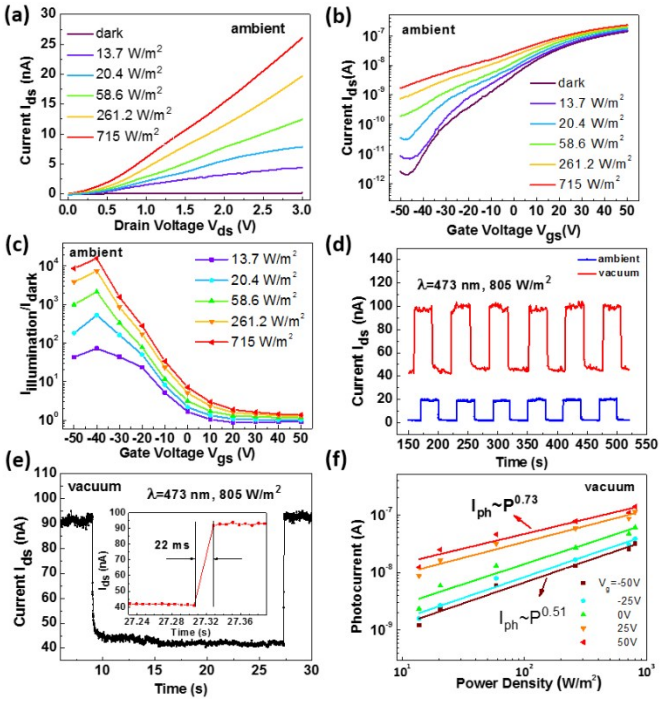

Fig. 4 Characteristics of a SnS_2 phototransistor illuminated under a 473 nm laser. (a and b) I_{ds}-V_{ds} (V_{gs} = 0 V) and I_{ds}-V_{gs} (V_{ds} = 3 V) curves of this device under different light intensity in ambient. (c) Plots of $I_{illumination}/I_{dark}$ (currents with/without illumination) ratio at different powers of incident light as a function of gate voltage. (V_{ds} = 3 V). (d) I-t curves in ambient and vacuum (V_{ds} = 3 V, V_{gs} = 0 V). (e) One time-resolved photoresponse cycle of the device in vacuum. Inset: photo switching rate of the photodetector. (f) Laser power dependence of the photocurrent (V_{ds} = 3 V, vacuum, the laser power density is 805 W/m^2).

Since the linear relationship between the photoresponse and the power of incident light is important, we plot the photocurrent as a function of the power of incident light at varied gate voltages in vacuum to exclude the impact of gas adsorptions. As depicted in Fig. 4f, the I_{ph} -*P* curves follow such a relationship: $I_{ph} \approx P^{\beta}$, where β increases from 0.51 to 0.73 as the gate voltage varied from -50 V to 50 V. The linear curves imply the photocurrent is determined by the amount of photogenerated carriers. However, the measured smaller value of β than the ideal factor 1 means there are loss of photocurrents. Since the varied temperature measurements and the theoretical calculations demonstrate the existence of sulfur vacancies, the recombination of photogenerated carriers is therefore considered to be induced by defects (sulfur vacancies) in the material.[5, 31, 40] Herein, we expect the photocurrents could be further increased by filling up the vacancy of sulfur in our SnS_2 NSs. We also calculate the responsivity (R_λ) from formulas as following: [34]

$$R_\lambda = I_{ph}/PS \quad (3)$$

$$EQE = hcR_\lambda/e\lambda \quad (4)$$

where I_{ph} is photocurrent, *P* is the incident light intensity and S is the effective illuminated area. As a result, R_λ and external quantum efficiency (EQE) is larger than 100 AW^{-1} and 33000% at *P* = 20.4 Wm^{-2}, V_{gs} = 50 V and V_{ds} = 3 V, which are thousands times higher than some phototransistors based on reported multilayer SnS_2, MoS_2, WSe_2 and black phosphorus, as shown in Table S1.

Conclusions

In conclusion, we develop a facile and fertile recipe to synthesize SnS_2 NSs on carbon cloth using a two-step CVD method. By transferring the NSs onto SiO_2/Si substrates, high sensitive phototransistors with on/off ratio surpassing 10^4 in ambient are fabricated. Low temperature measurements together with first-principles DFT calculations verify that sulphur vacancies in SnS_2 play a significant role in their electronic properties. By illuminating under a 473 nm laser, the device shows a sensitive response to the power density of illumination and a rising time as short as 22 ms in vacuum. Our work may pave a new pathway in the synthesis of LMDs and broaden the building blocks for high performance optoelectronic devices.

Experimental

Synthesis of SnS_2 NSs on carbon cloth.

SnS_2 NSs were grown on carbon cloth via a two-step CVD method in a horizontal vacuum tube furnace. Prior to the growth, carbon cloth needed to be ultrasonic cleaned by a mixed solution (ethanol: acetone: deionized water= 1:1:1) for at least 30 minutes. To grow SnO_2 nanowire, Sn powder (0.2 g, 99.8% Alfa) were placed in a quartz boat with a piece of 8 nm Au coated carbon cloth above it. After flushing with Ar gas three times and pumping to a vacuum lower than 1 Pa, it was heated to 850 ℃ in 17 minutes and kept for 1h under 140 standard centimeter cubic per minute (sccm) Ar and 1 sccm O_2. Afterwards, the furnace was naturally cooled to room temperature and 3D heterostructured SnO_2 nanowires were obtained. Then, SnS_2 NSs were synthesized using the as-grown SnO_2 nanowires and sulfur powder as precursor. In a typical growth process, S powder (0.6 g, 99.5% Alfa) was put at a cooler zone (120 °C) and as-grown SnO_2 nanowires at a hotter zone (630 °C). The heating process was finished in 30 minutes and kept for 1 h with 50 sccm Ar as carrier gas. After cooling to room temperature, stereoscopic hexagonal SnS_2 NSs were successfully acquired on the flexible carbon cloth.

Device fabrication and electrical measurement.

Thin SnS_2 NSs were drop-casted onto p-doped 300 nm SiO_2/Si substrates after ultrasonic oscillating carbon cloth in ethanol. After spin coating a layer of PMMA as a mask, the electrical metal electrodes were patterned by a standard e-beam lithography (EBL). Then Cr/Au (8 nm/60 nm) mental electrodes were deposited by thermal evaporation. All the electronic measurements were carried on a probe station (Lakeshore, TTP4) and a semiconductor characterization system (Keithley 4200). The light response of the phototransistor was measured under a 473 nm laser (RGBLase).

Theoretical calculation for defects.

The first-principles total energy and electronic structures calculations were performed in the framework of the density functional theory (DFT)[41, 42] within generalized gradient approximation (GGA) ,[43] as implemented in the Vienna ab initio simulation package (VASP) .[44-46] The frozen-core projector-augmented wave (PAW)[47] method and a plane-wave basis set with an energy cutoff of 400 eV were used in the calculations. For the calcualtions of defect formation energy, a 4x4x2 supercell was chosen and a Γ-center 2x2x2 k-mesh within the Monkhorst-Pack scheme[48] was used for Brillouin zone integration. In ordert to increase the accuracy of calcualted density of states (DOS), the k-mesh was further increased to 6x6x6, and the Gaussian smearing method with a smearing parameter of 0.05 eV was employed. In the atomic structure relaxation processes, all the atoms are allowed to relax until the quantum mechanical forces acting on them become less than 0.02 eV/ A.

The formation energies $\Delta H_f(\alpha, q)$ of defects are calculated as follows:[49, 50]

$$\Delta H_f(\alpha, q) = \Delta \mathrm{E}(\alpha, q) + \sum n_i \mu_i + q E_F, \qquad (5)$$

where

$$\Delta \mathrm{E}(\alpha, q) = \mathrm{E}(\alpha, \mathrm{q}) - \mathrm{E}(\mathrm{host}) + \sum n_i E_i + q \varepsilon_{VBM}(host). \quad (6)$$

E(host) is the totoal energy of host material and $\mathrm{E}(\alpha, \mathrm{q})$ is the total energy of the host material containing defect α in charge state q. The Fermi level E_F is referenced to the valence band maximum (VBM) of the host material and μ_i, determined by experimental conditions, is the chemical potential of element *i,* which is referenced to total energy E_i of its elemental solid/gas. n_i is the number of atoms of element *i* removed from or added to the host materials and q is the number of electrons transferred from the supercell to the reservoirs in forming the defect cell.

The transition energy $\varepsilon_\alpha^{q \to q'}$ is the Fermi energy at which the formation energy of defect α at charge state q is equal to that at charge state q'. According to the Eq. (4), the transition energy level with respect to the VBM can be obtained by:[50-51]

$$\varepsilon_\alpha^{q \to q'} = [\Delta E(\alpha, q) - \Delta E(\alpha, q')]/(q' - q) - \varepsilon_{VBM}(host) \quad (7)$$

Characterizations.

The thickness of the SnS_2 NSs were confirmed by an atomic force microscopy (AFM, Veeco Multimode). The surface images were captured by an electron scanning microscope (FESEM, Hitach S-4800). Raman spectroscopy (Renishaw InVia, 532 nm excitation laser) were used to confirm the synthesized NSs. The crystal quality of the SnS_2 NSs were examined by a transmission electron microscope (TEM, Tecnai F20).

Acknowledgements

This work at National Center for Nanoscience and Technology was supported by 973 Program of the Ministry of Science and Technology of China (No. 2012CB934103), the 100-Talents Program of the Chinese Academy of Sciences (No. Y1172911ZX), the National Natural Science Foundation of China (Nos. 21373065 and 61474033) and Beijing Natural Science Foundation (No. 2144059).The work at Institute of Semiconductors was supported by the National Natural Science Foundation of China under Grants No. 11474273, No. 11104264 and No. 61474116, and National Young 1000 Talents Plan.

Notes and references

1. S. Z. Butler, S. M. Hollen, L. Cao, Y. Cui, J. A. Gupta, H. R. Gutiérrez, T. F. Heinz, S. S. Hong, J. Huang, A. F. Ismach, E. Johnston-Halperin, M. Kuno, V. V. Plashnitsa, R. D. Robinson, R. S. Ruoff, S. Salahuddin, J. Shan, L. Shi, M. G. Spencer, M. Terrones, W. Windl and J. E. Goldberger, *ACS Nano*, 2013, **7**, 2898-2926.
2. D. Jariwala, V. K. Sangwan, L. J. Lauhon, T. J. Marks and M. C. Hersam, *ACS Nano*, 2014, **8**, 1102-1120.
3. G. Fiori, F. Bonaccorso, G. Iannaccone, T. Palacios, D. Neumaier, A. Seabaugh, S. K. Banerjee and L. Colombo, *Nat Nanotechnol.*, 2014, **9**, 768-779.
4. F. H. Koppens, T. Mueller, P. Avouris, A. C. Ferrari, M. S. Vitiello and M. Polini, *Nat Nanotechnol*, 2014, **9**, 780-793.
5. K. S. Novoselov, A. K. Geim, S. V. Morozov, D. Jiang, Y. Zhang, S. V. Dubonos, I. V. Grigorieva and A. A. Firsov, *Science*, 2004, **306**, 666-669.
6. X. Huang, Z. Yin, S. Wu, X. Qi, Q. He, Q. Zhang, Q. Yan, F. Boey and H. Zhang, *Small*, 2011, **7**, 1876-1902.
7. Z. Wang, K. Xu, Y. Li, X. Zhan, M. Safdar, Q. Wang, F. Wang and J. He, *ACS Nano*, 2014, **8**, 4859-4865.
8. M. M. Furchi, D. K. Polyushkin, A. Pospischil and T. Mueller, *Nano Lett.*, 2014, **14**, 6165-6170.
9. S. Ghatak, A. N. Pal and A. Ghosh, *ACS Nano*, 2011, **5**, 7707-7712.
10. G.-H. Lee, Y.-J. Yu, X. Cui, N. Petrone, C.-H. Lee, M. S. Choi, D.-Y. Lee, C. Lee, W. J. Yoo, K. Watanabe, T. Taniguchi, C. Nuckolls, P. Kim and J. Hone, *ACS Nano*, 2013, **7**, 7931-7936.
11. B. Radisavljevic and A. Kis, *Nat. Mater.*, 2013, **12**, 815-820.
12. K. Xu, F. Wang, Z. Wang, X. Zhan, Q. Wang, Z. Cheng, M. Safdar and J. He, *ACS Nano*, 2014, **8**, 8468-8476.
13. K. Xu, Z. Wang, X. Du, M. Safdar, C. Jiang and J. He, *Nanotechnology*, 2013, **24**, 465705.
14. W. Zhang, M.-H. Chiu, C.-H. Chen, W. Chen, L.-J. Li and A. T. S. Wee, *ACS Nano*, 2014, **8**, 8653-8661.
15. RadisavljevicB, RadenovicA, BrivioJ, GiacomettiV and KisA, *Nat. Nanotechnol.*, 2011, **6**, 147-150.
16. J. S. Ross, P. Klement, A. M. Jones, N. J. Ghimire, J. Yan, D. G. Mandrus, T. Taniguchi, K. Watanabe, K. Kitamura, W. Yao, D. H. Cobden and X. Xu, *Nat. Nanotechnol.*, 2014, **9**, 268-272.
17. C. Y. Fong and M. L. Cohen, *Phys. Rev. B*, 1972, **5**, 3095-3101.
18. J. Wang, M. Lundstrom, I. Electronic Devices Society Of and I. Electronic Devices Society Of, *Does source-to-drain*

tunneling limit the ultimate scaling of MOSFETs?, IEEE, New York, 2002.
19. H. Geng, Y. Su, H. Wei, M. Xu, L. Wei, Z. Yang and Y. Zhang, *Mater. Lett.*, 2013, **111**, 204-207.
20. Y. Zhao, Y. Zhang, L. Yao and M. Zhang, *Mater. Lett.*, 2014, **130**, 104-106.
21. S. Wang, S. Wang, J. Chen, P. Liu, M. Chen, H. Xiong, F. Guo and M. Liu, *J. Nanopart. Res.*, 2014, **16**.
22. S. Najmaei, Z. Liu, W. Zhou, X. Zou, G. Shi, S. Lei, B. I. Yakobson, J. C. Idrobo, P. M. Ajayan and J. Lou, *Nat. Mater.*, 2013, **12**, 754-759.
23. A. M. van der Zande, P. Y. Huang, D. A. Chenet, T. C. Berkelbach, Y. You, G. H. Lee, T. F. Heinz, D. R. Reichman, D. A. Muller and J. C. Hone, *Nat. Mater.*, 2013, **12**, 554-561.
24. H. Zhou, C. Wang, J. C. Shaw, R. Cheng, Y. Chen, X. Huang, Y. Liu, N. O. Weiss, Z. Lin, Y. Huang and X. Duan, *Nano Lett.*, 2014, DOI: 10.1021/nl504256y.
25. G. Su, V. G. Hadjiev, P. E. Loya, J. Zhang, S. Lei, S. Maharjan, P. Dong, P. M. Ajayan, J. Lou and H. Peng, *Nano Lett.*, 2015, **15**, 506-513.
26. J. Xia, D. Zhu, L. Wang, B. Huang, X. Huang and X. M. Meng, *Adv. Funct. Mater.*, 2015, just accepted.
27. H. Qiu, L. Pan, Z. Yao, J. Li, Y. Shi and X. Wang, *Appl. Phys. Lett.*, 2012, **100**, 123104.
28. H. Qiu, T. Xu, Z. Wang, W. Ren, H. Nan, Z. Ni, Q. Chen, S. Yuan, F. Miao, F. Song, G. Long, Y. Shi, L. Sun, J. Wang and X. Wang, *Nat. Commun.*, 2013, **4**, 2642.
29. Z. Yu, Y. Pan, Y. Shen, Z. Wang, Z. Y. Ong, T. Xu, R. Xin, L. Pan, B. Wang, L. Sun, J. Wang, G. Zhang, Y. W. Zhang, Y. Shi and X. Wang, *Nat. Commun.*, 2014, **5**, 5290.
30. Y. Huang, E. Sutter, J. T. Sadowski, M. Cotlet, O. L. A. Monti, D. A. Racke, M. R. Neupane, D. Wickramaratne, R. K. Lake, B. A. Parkinson and P. Sutter, *ACS Nano*, 2014, **8**, 10743-10755.
31. M. Buscema, D. J. Groenendijk, S. I. Blanter, G. A. Steele, H. S. J. van der Zant and A. Castellanos-Gomez, *Nano Lett.*, 2014, **14**, 3347-3352.
32. W. Choi, M. Y. Cho, A. Konar, J. H. Lee, G.-B. Cha, S. C. Hong, S. Kim, J. Kim, D. Jena, J. Joo and S. Kim, *Adv. Mater.*, 2012, **24**, 5832-5836.
33. N. Perea-López, A. L. Elías, A. Berkdemir, A. Castro-Beltran, H. R. Gutiérrez, S. Feng, R. Lv, T. Hayashi, F. López-Urías, S. Ghosh, B. Muchharla, S. Talapatra, H. Terrones and M. Terrones, *Adv. Funct. Mater.*, 2013, **23**, 5511-5517.
34. O. Lopez-Sanchez, D. Lembke, M. Kayci, A. Radenovic and A. Kis, *Nat. Nanotechnol.*, 2013, **8**, 497-501.
35. Z. Yin, H. Li, H. Li, L. Jiang, Y. Shi, Y. Sun, G. Lu, Q. Zhang, X. Chen and H. Zhang, *ACS Nano*, 2012, **6**, 74-80.
36. W. Zhang, J.-K. Huang, C.-H. Chen, Y.-H. Chang, Y.-J. Cheng and L.-J. Li, *Adv.Mater.*, 2013, **25**, 3456-3461.
37. I. P. Parkin, L. S. Price, T. G. Hibbert and K. C. Molloy, *J. Mater. Chem.*, 2001, **11**, 1486-1490.
38. D. De, J. Manongdo, S. See, V. Zhang, A. Guloy and H. Peng, *Nanotechnology*, 2013, **24**, 025202.
39. A. Ayari, E. Cobas, O. Ogundadegbe and M. S. Fuhrer, *J. Appl. Phys.*, 2007, **101**, 014507.
40. F. González-Posada, R. Songmuang, M. Den Hertog and E. Monroy, *Nano Lett.*, 2011, **12**, 172-176.
41. W. Kohn and L. J. Sham, *Phys. Rev.*, 1965, **140**, A1133-A1138.
42. P. Hohenberg and W. Kohn, *Phys. Rev.*, 1964, **136**, B864-B871.
43. J. P. Perdew, K. Burke and M. Ernzerhof, *Phys. Rev. Lett.*, 1996, **77**, 3865-3868.
44. G. Kresse and J. Hafner, *Phys. Rev. B*, 1993, **48**, 13115-13118.
45. G. Kresse and J. Furthmüller, *Comput. Mater. Sci.*, 1996, **6**, 15-50.
46. G. Kresse and J. Hafner, *Phys. Rev. B*, 1993, **47**, 558-561.
47. G. Kresse and D. Joubert, *Phys. Rev. B*, 1999, **59**, 1758-1775.
48. H. J. Monkhorst and J. D. Pack, *Phys. Rev. B*, 1976, **13**, 5188-5192.
49. S.-H. Wei and S. B. Zhang, *Phys. Rev. B*, 2002, **66**, 155211.
50. S.-H. Wei, *Comput. Mater. Sci.*, 2004, **30**, 337-348.
51. S.-H. Wei and S. B. Zhang, *Phys. Rev. B*, 2002, **66**, 155211.